Tunable Room Temperature Magnetic Skyrmions in Ir/Fe/Co/Pt Multilayers

Anjan Soumyanarayanan,[1,2,*] M. Raju,[1] A. L. Gonzalez Oyarce,[2] Anthony K. C. Tan,[1] Mi-Young Im,[3] A. P. Petrović,[1] Pin Ho,[2] K. H. Khoo,[4] M. Tran,[2] C. K. Gan,[4] F. Ernult,[2] and C. Panagopoulos[1,†]

[1]*Division of Physics and Applied Physics, School of Physical and Mathematical Sciences, Nanyang Technological University, 637371 Singapore*

[2]*Data Storage Institute, 2 Fusionopolis Way, 138634 Singapore*

[3]*Center for X-ray Optics, Lawrence Berkeley National Laboratory, Berkeley, California 94720, USA*

[4]*Institute of High Performance Computing, 1 Fusionopolis Way, 138632, Singapore*

Magnetic skyrmions are nanoscale topological spin structures offering great promise for next-generation information storage technologies. The recent discovery of sub-100 nm room temperature (RT) skyrmions in several multilayer films has triggered vigorous efforts to modulate their physical properties for their use in devices. Here we present a tunable RT skyrmion platform based on multilayer stacks of Ir/Fe/Co/Pt, which we study using X-ray microscopy, magnetic force microscopy and Hall transport techniques. By varying the ferromagnetic layer composition, we can tailor the magnetic interactions governing skyrmion properties, thereby tuning their thermodynamic stability parameter by an order of magnitude. The skyrmions exhibit a smooth crossover between isolated (metastable) and disordered lattice configurations across samples, while their size and density can be tuned by factors of 2 and 10 respectively. We thus establish a platform for investigating functional sub-50 nm RT skyrmions, pointing towards the development of skyrmion-based memory devices.

In conventional ferromagnets (FMs), the exchange interaction (A) aligns spins, and the anisotropy (K) determines energetically preferred orientations. Meanwhile, the Dzyaloshinskii-Moriya interaction[1,2] (DMI, D), generated by strong spin-orbit coupling (SOC) and broken inversion symmetry, induces a relative tilt between neighbouring spins. Magnetic skyrmions – finite-size two-dimensional (2D) 'whirls' of electron spin – form due to the competition between these 'winding' DMI and 'aligning' exchange interactions[3–7]. Skyrmions have several compelling attributes as prototype memory elements, namely their: (1) non-trivial spin topology, protecting them from disorder and thermal fluctuations[8–10], (2) small size and self-organization into dense lattices[5,6,11,12], and (3) solitonic nature, enabling particle-like dynamics, manipulation and addressability[10,12,13]. Originally magnetic skyrmions were discovered in non-centrosymmetric compounds hosting bulk DMI[4–7]. However, their emergence in thin multilayer films with interfacial DMI is particularly exciting[14,15] due to the inherent tunability of magnetic interactions in 2D, and the material compatibility with existing spintronic technology[8].

The DMI generated at interfaces between ultrathin FM layers and strong SOC metals[15–19] can host Néel-textured skyrmions, first observed in epitaxial monolayers of Fe on Ir(111)[11,12]. While such ultrathin films can stabilise small skyrmions (∼8 nm) only at low temperatures (< 30 K), analogous multilayer films have recently been shown to host ∼50-100 nm RT skyrmions[20–22]. Here, a FM layer (e.g. Co) is sandwiched between different SOC metals (e.g. Pt and Ir/Ta) to produce a net effective DMI[20–22], and multiple repeats of such trilayers stabilise columnar skyrmions through interlayer exchange coupling[23,24]. Multilayer skyrmions have been imaged using synchrotron-based microscopy techniques[20–22], with recent demonstrations of their confinement[20,22], nucleation and dynamics[21,25,26] in constricted geometries. To translate these attributes into functional RT devices, we must first develop methods of controlling and varying the physical properties of skyrmions, such as their thermodynamic stability, size and density.

Individual skyrmion addressability will be particularly important for technological applications. To realise this, we must achieve control over the skyrmion stability via the critical material parameter, κ[3,16,27–29]:

$$\kappa = (4/\pi) \cdot D/\sqrt{A \cdot K} \equiv D/D_c \,, \qquad (1)$$

similar to the well-known Ginzburg-Landau parameter for superconducting vortices. For $\kappa > 1$, skyrmions are thermodynamically stable entities which form a lattice at equilibrium, while for $0 < \kappa < 1$, they would be metastable, isolated particles[27–29]. It is also important to establish a route towards reducing the skyrmion size at RT, thereby maximising its potential for energy-efficient, high-density memory. Furthermore, the ability to control skyrmion density would enable device performance tuning in both static[9] and dynamic[30,31] configurations. Investigating the technological relevance of multilayer skyrmions will also necessitate their electrical detection[32–34] and imaging[35] within stack configurations translatable to practical devices.

Here we describe our development of a new material platform – multilayer stacks of Ir/Fe/Co/Pt – as a host of sub-50 nm skyrmions with continuously tunable properties. By harnessing the large and opposite signs of DMI generated from Fe/Ir[11] and Co/Pt[19] interfaces, we achieve substantial control over the effective DMI governing skyrmion properties. We first con-

firm the presence of nanoscale RT skyrmions via established X-ray microscopy techniques, and investigate their field evolution using magnetic force microscopy (MFM) and Hall transport. By varying FM layer composition and thickness, we control D and K, thereby modulating the skyrmion stability parameter κ by an order of magnitude, the skyrmion size by a factor of 2, and the skyrmion density by a factor of 10. We thus establish a platform for realising tunable, functional RT skyrmions in multilayers, and demonstrate how they may be studied using commonly available lab-based techniques.

Multilayer Stack Structure

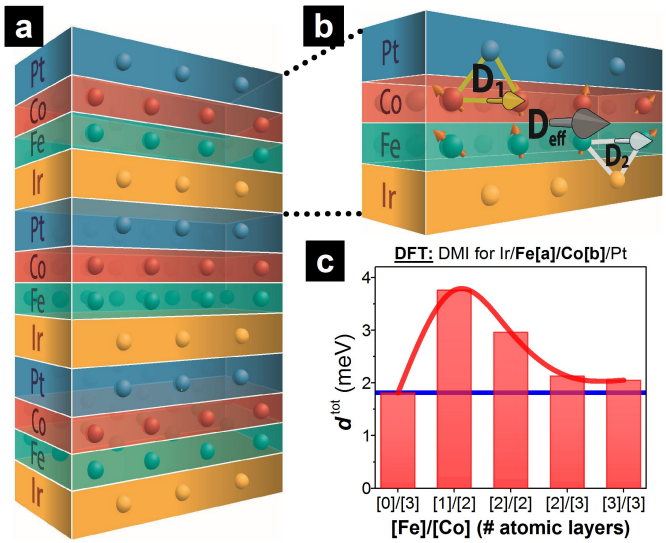

FIG. 1. **DMI Enhancement in Ir/Fe/Co/Pt. (a)** Schematic of our multilayer stacks, featuring several repeats of a sequence of Ir, Fe, Co, and Pt layers. **(b)** Magnified schematic of the Ir/Fe/Co/Pt stack, showing large DMI vectors of opposite sign at Co/Pt (top, $\vec{D}_1$) and Fe/Ir (bottom, $\vec{D}_2$) interfaces, acting in concert to enhance the effective DMI, $\vec{D}_{\text{eff}}$. **(c)** DFT calculation of the DMI (d^{tot}, in meV) for Ir[3]/Fe[a]/Co[b]/Pt[3] stacks with varying Fe/Co composition (number of atomic layers in braces), with DMI enhancement upon Fe addition.

The interfacial DMI is defined for neighbouring spins $\vec{S}_{1,2}$ as

$$\mathcal{H}_{\text{DMI}} = \vec{D}_{12} \cdot (\vec{S}_1 \times \vec{S}_2) \tag{2}$$

The magnitude and sign of $\vec{D}_{12}$, determined by the FM and SOC layers at the interface, govern the phenomenology of multilayer skyrmions[7,8]. Notably, the Co/Pt interface hosts a ***large, positive DMI*** ($d^{\text{tot}}_{\text{Co-Pt}} \sim +3$ meV), enabling Co-based trilayers with large DMI (Co/Pt) and small DMI (e.g. Co/Ir[20], Co/MgO[22], Co/Ta[21] etc.) interfaces to host skyrmions. Meanwhile, the Fe/Ir interface hosts a ***large, negative DMI*** ($d^{\text{tot}}_{\text{Fe-Ir}} \sim -2$ meV)[11,18,19,36]. Therefore, a stack structure combining the Co/Pt and Fe/Ir interfaces, with large DMI of opposite sign, could exhibit an additively enhanced effective DMI. Here we examine such a four-layer Ir/Fe/Co/Pt stack (Fig. 1a-b) and establish it as a platform for tailoring magnetic interactions and skyrmion properties.

To validate our hypothesis of DMI enhancement, we performed *ab initio* density functional theory (DFT) calculations on the Ir/Fe/Co/Pt stack (Fig. 1b) with varying Fe/Co composition. The effective DMI, d^{tot} (in meV) was determined from the difference between the DFT calculated energies for clockwise and counter-clockwise chiral spin configurations, following the work of Yang *et al.*[19,22] (see Methods), and is shown in Fig. 1c (number of atomic layers in braces). For the same total FM thickness (e.g. Fe[0]/Co[3]) vs. Fe[1]/Co[2]), we observe a substantial ($\sim$ 100%) DMI enhancement with the incorporation of an Fe layer. In fact, even for larger FM thicknesses, e.g. Fe[2]/Co[2], the DMI enhancement relative to Fe[0]/Co[3] is $\sim$ 50%, reducing monotonically with thickness. During the preparation of this manuscript, we became aware of a DFT report of similar DMI enhancement for one such composition (Fe[1]/Co[2])[37]. Importantly, increasing the Fe/Co ratio and the overall FM thickness would also result in reduced anisotropy (K_{eff}). This could enable continuous modulation of both D and K, offering direct control over skyrmion properties.

Multilayer films with [Ir(10)/Fe(x)/Co(y)/Pt(10)]$_{20}$ stacks (layer thickness in Å, in parentheses) were sputtered on thermally oxidised Si wafers with optimised film texture and interface quality, and on Si_3N_4 membranes for X-ray microscopy (see Methods). The thickness of Fe (x : 0-6 Å) and Co (y : 4-6 Å) layers were varied across the films, and the samples studied are described in terms of their **Fe(x)/Co(y)** composition. While the results detailed here were measured in films with 20 stack repeats for enhanced X-ray contrast, similar trends were observed with transport and MFM in samples with 8 repeats. The data presented here were acquired following saturation at positive fields ($H > +|H_S|$) in out-of-plane (OP) configuration. The OP magnetisation ($M(H)$) loops for these stacks have a characteristic sheared shape (see e.g. Fig. 2j), which is typically a signature of labyrinth domain states[21].

Microscopic Imaging of RT Skyrmions

Fig. 2 shows representative images acquired by three different magnetic microscopy experiments in varying OP fields for sample **Fe(3)/Co(6)**. We begin by examining magnetic transmission soft X-ray microscopy (MTXM - a technique previously used to study multilayer skyrmion films[21]) images acquired using films grown on Si_3N_4 membranes (see Methods). Data recorded at the Co L_3 edge (778 eV) (Fig. 2a-c) show that as the field is reduced from $+H_S$, round-shaped sub-100 nm features with negative (blue) contrast emerge (Fig. 2a), which grow to form elongated labyrinthine domains at zero field (Fig. 2b). At negative fields, these domains give way to round-shaped features with positive (yellow) contrast (Fig. 2c), which shrink and dis-

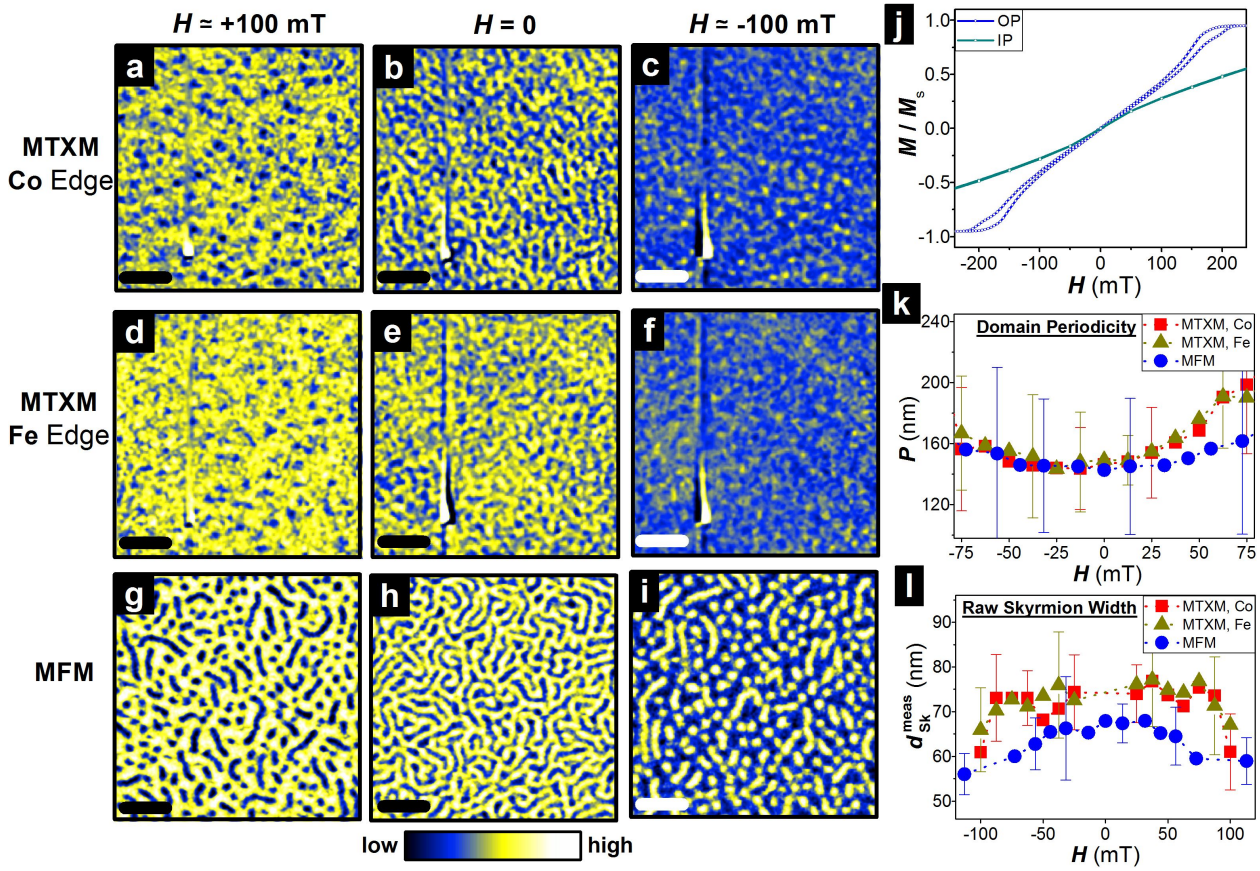

FIG. 2. **Magnetic Microscopy of RT Skyrmions. (a-i)** Microscopic imaging (scale bar: 0.5 μm) of sample **Fe(3)/Co(6)** at RT with MTXM (on Si_3N_4 membrane) at the Co L_3 edge (a-c), MTXM at the Fe L_3 edge (d-f), over the same sample region as (a-c), and MFM (SiO_2 substrate, g-i). Images shown are acquired at $\sim +100$ mT (a, d, g), 0 T (b, e, h) and ~ -100 mT (c, f, i) respectively after saturation at $\sim +250$ mT, and display similar evolution in magnetic contrast with applied field. A dead pixel on the MTXM CCD (a-f: bottom left) does not affect our analysis. **(j)** Hysteresis loops for out-of plane (OP, blue) and in-plane (IP, green) magnetisation, M/M_S. **(k-l)** Comparisons of the field-dependent trends of magnetic domain periodicity, P (k) and *raw* (as measured) skyrmion width d_{Sk}^{meas} (l), using MTXM - Co (red), MTXM - Fe (green) and MFM (blue) images respectively. Representative error bars are indicated (see Methods).

appear at $-H_S$. Based on the sub-100 nm size, aspect ratio, and field evolution of these magnetic features, and in light of X-ray microscopy work on similar multilayers[20–22], we identify them as Néel skyrmions. In contrast to known multilayer skyrmion hosts[20–22], Ir/Fe/Co/Pt stacks include an additional FM layer (Fe). This enables us to corroborate our observations by performing analogous MTXM experiments at the Fe L_3 edge (708 eV, Fig. 2d-f), over the same sample region as Fig. 2a-c. While the magnetic contrast is diminished (c.f. Fig. 2a-c), analogous magnetic textures persist with a comparable field evolution. Importantly, the measured magnetic domain periodicity and skyrmion size (d_{Sk}^{MTXM}) show excellent agreement across these two experiments (Fig. 2k-l, see Methods), confirming that skyrmionic spin textures persist across the composite (Co/Fe) FM layer.

To facilitate direct comparison with electrical transport experiments, we next used MFM to image similar stacks deposited on Si/SiO_2 wafers. Our MFM measurements were performed using ultra-low moment tips (diameter ∼30 nm) for non-perturbative imaging with high spatial resolution (see Methods). Representative MFM results for sample **Fe(3)/Co(6)** are shown in Fig. 2g-i. The field evolution is similar to MTXM, while displaying markedly higher magnetic and spatial contrast: skyrmions are clearly visible at higher fields (Fig. 2g, i), compared with stripes at zero field (Fig. 2h). Despite the difference in substrates (Si/SiO_2 for MFM vs. Si_3N_4 membranes for MTXM), the domain periodicity from MFM (Fig. 2k, blue) shows similar magnitude and field evolution trends as the MTXM results.

Finally, in Fig. 2l we compare the measured skyrmion size d_{Sk}^{meas} as a function of applied field, across all three experiments. The values of d_{Sk}^{meas} correspond to the observed (raw) skyrmion size for each technique, obtained from 2D Gaussian fits to raw data. No deconvolution has been performed to account for the X-ray point spread function or MFM tip size. All three experiments display the expected trend of reducing d_{Sk}^{meas} with increasing field. The MTXM results (d_{Sk}^{MTXM}) show good agreement between the Co and Fe experiments, and the

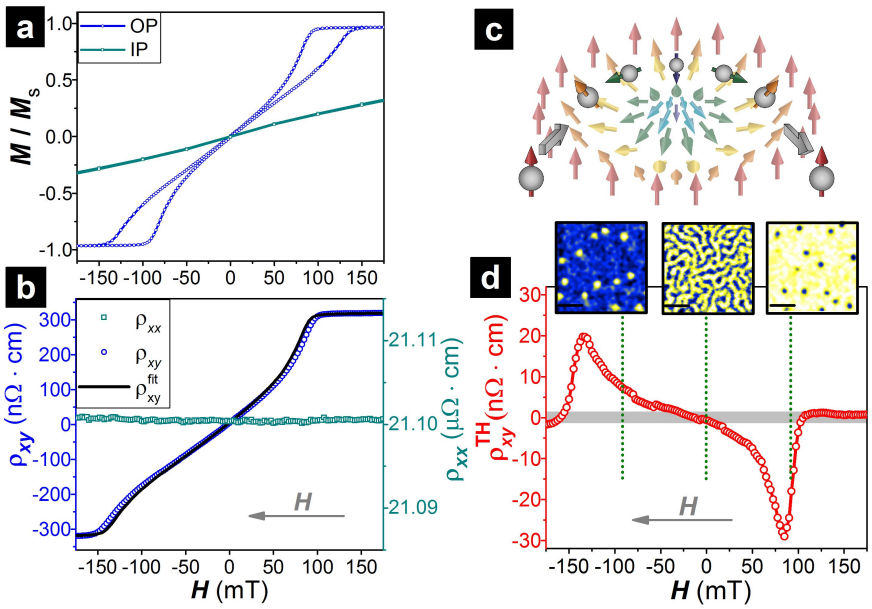

FIG. 3. **Topological Hall (TH) Effect from RT Skyrmions. (a)** OP (blue) and IP (green) magnetisation, M/M_S, and (b) longitudinal (ρ_{xx}, green) and Hall (ρ_{xy}, blue) resistivity as a function of applied field (grey arrow indicates sweep direction), for sample **Fe(2)/Co(6)** at RT. The black line (ρ_{xy}^{fit}) is a fit to ρ_{xy}, accounting for conventional and anomalous Hall effects (Eqn. 3,[38]). **(c)** Schematic TH effect from Néel skyrmions, resulting from the Berry phase accumulated by 2π spin rotation of itinerant electrons adiabatically traversing the skyrmion spin texture. **(d)** Residual Hall signal ρ_{xy}^{TH}, corresponding to TH effect from skyrmions, obtained from (b) as $\rho_{xy}^{\text{TH}}(H) = \rho_{xy}(H) - \rho_{xy}^{\text{fit}}(H)$. Insets show MFM images (scale bar: 0.5 μm) acquired at fields corresponding to dashed green lines, indicating the magnetic structures that generate the TH signal.

MFM results also agree reasonably well with MTXM, albeit with a systematic offset of ∼10 nm. We expect both MTXM and MFM probes to overestimate the true skyrmion size to varying extents, due to differences in probe sizes and substrates. Nevertheless, the excellent agreement between the $d_{\text{Sk}}^{\text{meas}}$ trends firmly establishes MFM as a reliable tool for imaging RT skyrmions.

Unconventional Anomalous Hall Effect

To determine the electrical signature of Néel skyrmions, high-resolution magnetotransport measurements were performed on the films using small, non-perturbative current densities (as low as 10^4 A/m^2). Great care was taken to eliminate any field offsets between the transport data (Fig. 3b) and complementary magnetisation measurements (Fig. 3a, see Methods). The typical RT transport characteristics for Ir/Fe/Co/Pt stacks (representative sample **Fe(2)/Co(6)**) are shown in Fig. 3b, with the longitudinal resistivity ($\rho_{xx}(H)$) constant to 0.02% within the field range of interest. The Hall resistivity data ($\rho_{xy}(H)$, Fig. 3b) was analysed by accounting for contributions from the conventional ($\propto H$) and anomalous ($\propto M(H)$) Hall effects[38]:

$$\rho_{xy}^{\text{fit}}(H) = R_0 \cdot H + \Big(A \cdot \rho_{xx}(H) + B \cdot \rho_{xx}^2(H)\Big) \cdot M(H) \tag{3}$$

Here, R_0 is the Hall coefficient, while A and B represent contributions from skew and side-jump scattering mechanisms respectively. After accounting for these contributions, a residual Hall signal, $\rho_{xy}^{\text{TH}}(H) = \rho_{xy}(H) - \rho_{xy}^{\text{fit}}(H)$, clearly emerges with a maximum value of ∼ 30 nΩ-cm (Fig. 3d). This is comparable in magnitude to previous studies of bulk DMI materials[32,34,39], where the observed $\rho_{xy}^{\text{TH}}(H)$ (2-100 nΩ-cm) has been attributed to Bloch skyrmions[32,34,39]. Moreover, the field range corresponding to finite $\rho_{xy}^{\text{TH}}(H)$, as well as the $\rho_{xy}^{\text{TH}}(H)$ peak position, are in agreement with the field range in which skyrmions are observed by MFM (Fig. 3d insets) and MTXM experiments. Based on the consistency and reproducibility of $\rho_{xy}^{\text{TH}}(H)$ across several Ir/Fe(x)/Co(y)/Pt stacks, we ascribe its origin to the ***topological Hall (TH) effect*** from Néel skyrmions.

The TH effect results from the Berry phase accumulated by itinerant electrons crossing the 2D skyrmion spin texture (Fig. 3c). The $\rho_{xy}^{\text{TH}}(H)$ profile has a characteristic hump shape – weak at low field due to the predominance of 1D stripes (Fig. 3d, centre inset), with a peak at higher field due to skyrmion proliferation (Fig. 3d, left/right insets), which disappears at saturation[32,34,40]. A key contrast with $\rho_{xy}^{\text{TH}}(H)$ in Bloch skyrmion materials[34,39] is the observed asymmetry through the field sweep: $\left|\rho_{xy}^{\text{TH}}(+H)\right| \neq \left|\rho_{xy}^{\text{TH}}(-H)\right|$. Such asymmetry is likely due to hysteretic domain formation driven by the interfacial anisotropy in our multilayers. This is the first observed electrical signature of RT Néel skyrmions, establishing the utility of Hall transport towards RT skyrmion detection in devices.

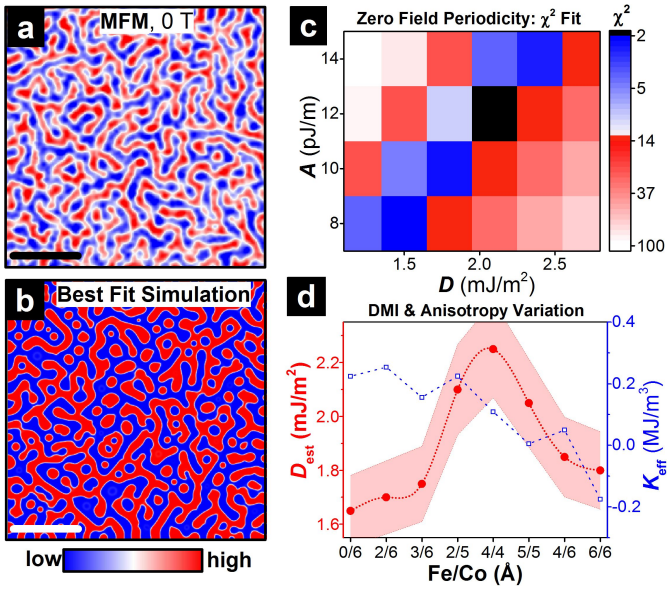

FIG. 4. **DMI Enhancement with Fe/Co Composition. (a-b)** MFM image (a) and best-fit micromagnetic simulation (b) (scale bar: 0.5 μm) of the zero field magnetic contrast for sample **Fe(2)/Co(5)**. **(c)** A χ^2-fit comparison of the magnetic domain periodicity between MFM data (a) and micromagnetic simulations, with parameters A and D varied over a range of likely values. The best fit corresponds to $A_{\text{est}} = 12$ pJ/m, $D_{\text{est}} = 2.1$ mJ/m^2. **(d)** The best-fit DMI, D_{est}, obtained using the method in (c), for the samples studied in this work (shaded region indicates error bars) – found to be largest for **Fe(4)/Co(4):** $D_{\text{est}} = (2.25 \pm 0.2)$ mJ/m^2.

DMI Enhancement

Having confirmed the presence of RT skyrmions, we examine the effects of varying **Fe(x)/Co(y)** composition on the magnetic interactions governing skyrmion properties. While K_{eff} can be determined directly from magnetisation measurements, D was estimated by comparing the magnetic domain periodicity (determined by Fourier analysis) in zero field MFM images (Fig. 4a, for **Fe(2)/Co(5)**) with corresponding micromagnetic simulations (Fig. 4b, see Methods)[20,21]. A and D were varied over a range of likely values to find the best fit parameters, determined using a 2D χ^2 fit (Fig. 4c). Across the range of samples, the best fits consistently indicate $A_{\text{est}} = 12$ pJ/m, in agreement with results on similar multilayers[20,21]. In contrast, D_{est} shows a systematic "dome"-like variation of $\sim 50\%$, ranging from $1.6 - 2.3$ mJ/m^2 (Fig. 4d, red), while K_{eff} decreases with increasing Fe/Co ratio and FM thickness (Fig. 4d, blue).

The DMI enhancement for Fe($x > 0$) relative to **Fe(0)/Co(6)** (Ir/Co/Pt) is consistent with DFT calculations (Fig. 1c). The inclusion of Fe results in the gradual formation of a Fe/Ir interface and corresponding suppression of the Co/Ir boundary, leading to increasing DMI. The DMI reaches its maximal value for complete monolayer coverage at both Fe/Ir and Co/Pt interfaces (near **Fe(4)/Co(4)**), and reduces as the FM layer thickness is further increased due to its interfacial nature. Crucially, the "dome"-like variation in D_{est} does not track the observed decreasing trend in K_{eff} (Fig. 4d, blue) – the latter decreases monotonically with increasing Fe/Co ratio and FM thickness. This indicates that a degree of independent variation in D_{est} and K_{eff} can be achieved within our samples. We also note that our peak $D_{\text{est}} = (2.25 \pm 0.2)$ mJ/m^2 (for **Fe(4)/Co(4)**) is larger than values reported for other multilayer skyrmion hosts[20–22].

Tuning Skyrmion Stability

The observed variation of D_{est} and K_{eff} has direct implications for the physical properties of our skyrmions, whose stability, size and density evolve visibly across our samples (Fig. 5b-e). First, the thermodynamic stability parameter, κ_{est} ($\equiv D_{\text{est}}/D_{\text{c}}$, Eqn. 1, see Methods) varies smoothly from ~ 0.7 to ~ 7 (Fig. 5a). This order of magnitude variation has a dramatic effect on the spatial skyrmion configurations at maximal density ($H \sim -0.8\, H_{\text{S}}$, Fig. 5b-e), which can be analysed using Delaunay triangulation statistics (details in §S4) for the nearest neighbor (NN) coordination number (N_{NN}, Fig. 5f) and angular orientation (θ_{NN}, Fig. 5g)[41]. For $\kappa_{\text{est}} < 1$ (Fig. 5f-g, bottom plots), the distributions show a large spread, with a marked deviation from ordered configurations, and correspond to metastable, isolated skyrmions (circular FT, Fig. 5c inset). In contrast, for $\kappa_{\text{est}} > 1$, the distributions gradually converge around $N_{\text{NN}} = 6$, $\theta_{\text{NN}} = 60°$ – forming a disordered hexgonal skyrmion lattice (Fig. 5e inset). The crossover between isolated and lattice configurations appears to be smooth, possibly due to the granularity of magnetic properties and disorder pinning effects in sputtered films. Such a gradual crossover would likely enable the skyrmion stabilisation over a wider range of sizes and densities, while maintaining individual addressability.

Tuning Skyrmion Size & Density

Fig. 6a details the field dependence of skyrmion size, $d_{\text{Sk}}^{\text{MFM}}$, for three samples: $d_{\text{Sk}}^{\text{MFM}}$ consistently falls with increasing field[20–22]. Skyrmions in **Fe(4)/Co(4)** ($D_{\text{est}} \simeq 2.25$ mJ/m^2, $d_{\text{Sk}}^{\text{MFM}} \sim$ 40-55 nm) are considerably smaller than in **Fe(2)/Co(6)** ($D_{\text{est}} \simeq 1.65$ mJ/m^2, $d_{\text{Sk}}^{\text{MFM}} \sim$ 75-100 nm) or **Fe(4)/Co(6)** ($D_{\text{est}} \simeq 1.85$ mJ/m^2, $d_{\text{Sk}}^{\text{MFM}} \sim$ 50-60 nm). This is a consequence of DMI enhancement in **Fe(4)/Co(4)** ($\kappa_{\text{est}} \simeq 1.5 > 1$), which induces a faster spatial spin rotation relative to **Fe(2)/Co(6)**, resulting in a large ($\sim 2\times$) reduction in skyrmion size. The influence of DMI on skyrmion geometry is evident from the trend in $d_{\text{Sk}}^{\text{MFM}}$ across all our samples (Fig. 6b), which shows a prominent minimum at **Fe(4)/Co(4)**, and visible anti-correlation with the "dome"-shaped variation in DMI (Fig. 4d). Note that the error bars for $d_{\text{Sk}}^{\text{MFM}}$ (Fig. 6a-b) represent a true spread in the observed size of multiple

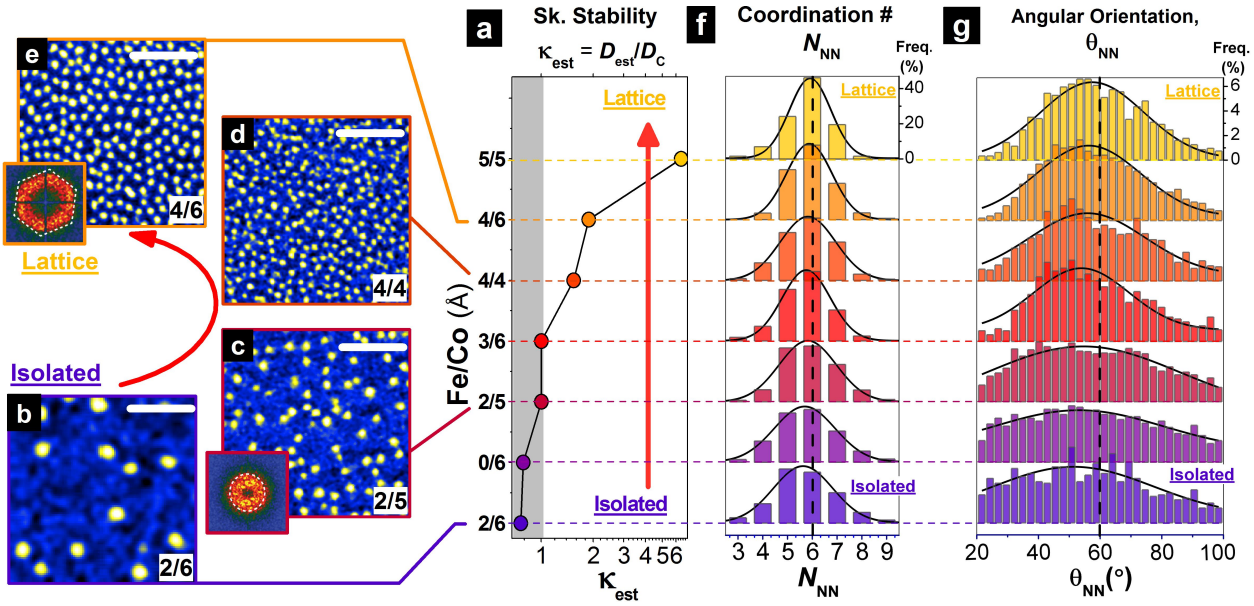

FIG. 5. **Tuning Skyrmion Stability with Fe/Co Composition.** **(a)** Evolution of the stability parameter $\kappa_{est} \equiv D_{est}/D_c$ from $\sim 0.7 - 7.0$ across our samples. **(b-e)** MFM images (scale bar: 0.5 μm) of skyrmion configurations at $H \sim -0.8\, H_S$ (max. density), for samples **Fe(2)/Co(6)** (b), **Fe(2)/Co(5)** (c), **Fe(4)/Co(4)** (d), and **Fe(4)/Co(6)** (e) respectively. With increasing κ, the configuration evolves from sparse, isolated particles (b) to a dense, disordered lattice (e), with visible variations in skyrmion size. The short-range hexagonal order in (e) is evident from the hexagonal Fourier transform (FT, inset), in contrast to the circular FT for (c) (inset). **(f-g)** Quantitative analysis of skyrmion configuration across samples, using Delaunay triangulation (details in §S4) to determine nearest neighbor (NN) statistics (min. sample size: 150 skyrmions): (f) NN coordination number, N_{NN}, and (g) NN angular orientation, θ_{NN}. With increasing κ, the distributions converge around $N_{NN} = 6$ and $\theta_{NN} = 60°$ (hexagonal lattice).

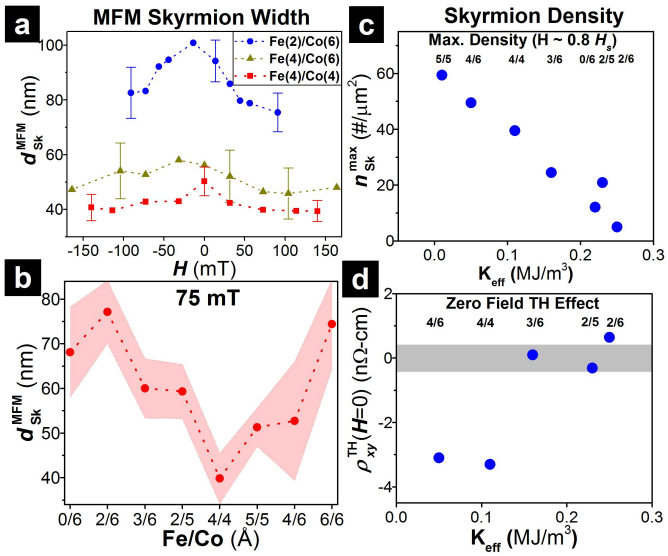

FIG. 6. **Tuning Skyrmion Properties with Fe/Co Composition.** **(a)** Field dependence of the MFM skyrmion width (d_{Sk}^{MFM}) for samples **Fe(2)/Co(6)** ($D_{est} \simeq 1.65$ mJ/m^2, blue), **Fe(4)/Co(6)** ($D_{est} \simeq 1.85$ mJ/m^2, green), and **Fe(4)/Co(4)** ($D_{est} \simeq 2.25$ mJ/m^2, red). **(b)** Variation of d_{Sk}^{MFM} across samples at $H \simeq 75$ mT, showing a prominent dip for **Fe(4)/Co(4)** ($d_{Sk}^{MFM} \simeq (39.8 \pm 5.6)$ nm) and a visible anti-correlation with D_{est} (Fig. 4d). **(c)** Variation of skyrmion density, n_{Sk} with K_{eff}, as measured across samples at $H \simeq 0.8\, H_S$. **(d)** Zero field TH signal ($\rho_{xy}^{TH}(H = 0)$), indicative of zero field skyrmion density, as a function of K_{eff} across several samples. Corresponding Fe/Co sample compositions for (c-d) are indicated at the top.

skyrmions in our films, consistent with reports in confined geometries[21]. Finally, we re-emphasise that the "raw" d_{Sk}^{MFM} values reported here (e.g. $d_{Sk}^{MFM} \simeq (39.8 \pm 5.6)$ nm for **Fe(4)/Co(4)** at 75 mT) overestimate the true skyrmion size, due to the absence of any probe deconvolution from our ~30 nm tips. In fact, RT skyrmions in **Fe(4)/Co(4)** could be considerably smaller than any multilayer skyrmions reported so far[20–22].

While DMI controls the skyrmion size, the variation in K_{eff} governs the skyrmion density n_{Sk} at a given field. Fig. 6c shows the maximum skyrmion density n_{Sk}^{max} (for $|H| \lesssim \pm 200$ mT), as a function of K_{eff} across our samples. As K_{eff} is reduced from strongly OP (~0.3 MJ/m^3) to near-IP ($\sim$ 0 MJ/m^3), n_{Sk}^{max} shows a dramatic increase: from $\sim$ 5 /μm^2 to $\sim$ 60 /μm^2. Skyrmions in low K_{eff} samples are stable over a broader range of fields ($> \pm 0.2$ T), due to increased H_S, and are also nucleated close to zero field with much greater ease. The increased presence of near zero field skyrmions in low K_{eff} samples is also reflected in Hall measurements, specifically in the TH signal at zero field, $\rho_{xy}^{TH}(H = 0)$ (Fig. 6d): negligible for high K_{eff}, but substantially larger in magnitude for low K_{eff} samples. Varying K_{eff} on either side of the optimal DMI composition is a route towards engineering stacks with the requisite skyrmion density and stability for specific applications.

Summary and Outlook

We have synthesised magnetic multilayer stacks hosting RT skyrmions with tunable properties. By varying

the Fe/Co composition, we have enhanced the DMI by $\sim$ 50% and also varied K_{eff}, thereby continuously tuning the thermodynamic stability parameter, κ_{est}, over an order of magnitude. The resulting skyrmion configuration, imaged by X-ray microscopy and MFM, evolves from isolated, metastable particles to a disordered hexagonal lattice. Modulating D_{est} and K_{eff} enables us to vary the skyrmion size (by 2×), density (by 10×) and ease of nucleation. This demonstration of a platform for tunable sub-50 nm RT skyrmions and their electrical detection via Hall transport has immediate relevance for device applications.

The myriad proposals of skyrmion-based memory devices predominantly build upon either (a) the nucleation or deletion of single skyrmions in nanostructures[8,9,28], or (b) the dynamics of a train of skyrmions in a racetrack configuration[30,42,43]. The material requirements for (a) would be geared towards the use of individual, isolated skyrmions in confined geometries. In contrast, optimal materials for devices based on (b) would correspond to dense arrays of skyrmions, ideally in an ordered configuration, for high-speed readout and increased mobility. As demonstrated here, Ir/Fe/Co/Pt stacks can directly address both these contrasting requirements of skyrmion properties by simply varying the stack composition. Crucially, the smooth crossover between isolated and lattice configurations with composition can simultaneously enable stabilisation and individual addressability for a wide range of skyrmion sizes and densities. We thus provide a material platform for fast-tracking technological explorations of skyrmion-based memory devices.

Methods

Film Deposition. Multilayer films consisting of:
Ta(30)/Pt(10)/[**Ir(10)/Fe(0-6)/Co(4-6)/Pt(10)**]$_{20}$/Pt(20)
(layer thickness in Å in parentheses) were deposited on thermally oxidised 100 mm Si wafers by DC magnetron sputtering at RT, using a Chiron™ UHV system (base pressure: 1×10^{-8} torr) manufactured by Bestec GmbH. The films were simultaneously deposited on Si_3N_4 membranes (thickness: 200 nm) for MTXM measurements, and the Ir/Fe/Co/Pt stack was repeated 20 times to enhance the XMCD contrast. Further deposition and characterisation details are in §S1.

MTXM (X-Ray Microscopy) Experiments were performed for several Fe/Co compositions on multilayers deposited on Si_3N_4 membranes. The data were acquired in OP geometry, with the sample plane normal to the propagation direction of circularly polarized X-ray beam, using full-field MTXM at the Advanced Light Source (XM-1 BL 6.1.2). The samples were saturated OP at $\sim$ +250 mT, and MTXM images were acquired through hysteresis loops at the Co L_3 edge ($\sim$778 eV), and in some cases, at the Fe L_3 edge ($\sim$708 eV) over the same sample region. The spatial length scales observed at the Co and Fe edges were calibrated using standard samples, and the Fe data were corrected for a $\sim$ 7% CCD camera magnification artefact.

MFM Experiments were performed using a NX-10 AFM/MFM manufactured by Park Systems™. All data were acquired in ambient conditions, with the MFM mounted on a vibration-isolated platform. The MFM tips used (SSS-MFMR) were $\sim$ 30 nm in diameter, with ultra-low magnetic moments ($\sim$80 emu/cm^3), optimised for non-perturbative magnetic imaging with high spatial resolution. The samples were saturated OP using fields up to 0.5 T, and measurements were performed in OP fields of up to 0.2 T. The zero field results reported here were quantitatively consistent with those obtained after AC demagnetisation. Precautions were taken to eliminate tip-induced perturbations, drift, and other artefacts, and the results obtained were reproduced several times for consistency.

Magnetisation, $M(H)$, of the films was determined using SQUID magnetometry, with a Quantum Design™ Magnetic Properties Measurement System (MPMS).

Electrical Transport. The magnetoresistance and Hall coefficients were measured using a lock-in technique (excitation frequency: 0-300 Hz), enabling sub-nV resolution (details in §S3). The measurements were performed using a custom-built variable temperature insert (VTI) housed in a high-field magnet, complemented by a Quantum Design™ Physical Properties Measurement System (PPMS). The data reported here were acquired through a full hysteresis cycle, with 25 Oe steps within $\pm H_S$ after saturation at large fields (+4 T), using small current densities (as low as 10^4 A/m^2) so as to not perturb the spin textures (consistency checks in §S3). Importantly, the Hall data were analysed after carefully accounting for any magnetic field offsets between magnetisation (Fig. 3a) and transport (Fig. 3b) measurements. To this end, repeated field calibrations were performed on each of the instruments using reference samples.

Density Functional Theory Calculations. To compute the DMI, we performed first-principles DFT calculations using the technique employed by Yang *et al.*[19]. The multilayer stack, Ir[3]/Fe[b]/Co[a]/Pt[3] (number of atomic layers in braces), were set up and separated by a vacuum of 10 Å along the OP direction, with the IP lattice constants set to the calculated bulk Ir value. Next, DMI was considered only between intralayer NN atoms to a first approximation, and used to define $d^{\text{tot}} = \sum_k d^k$, i.e. the sum of DMI coefficients, d^k, for each layer[19]. Subsequently, clockwise and anti-clockwise spin spirals were constructed across a supercell using the constrained spin method. The energy difference between these two configurations was computed and scaled by a geometry and spin-spiral dependent factor to obtain d^{tot} (Fig. 1c). Further procedural details are in §S2.

Micromagnetic Simulations were performed using the mumax^3 software package[44], which accounts for interfacial DMI. The multilayers were modelled with a mesh size of 4×4 nm^2 over a 2×2 μm^2 area for comparison with films. The z length of the discretisation mesh was changed to match the sample's magnetic layer thickness, with the non-magnetic spacer approximated to a single layer thickness. The stack configuration used (20 repeats) was consistent with experiments, and the M_S and K_{eff} values used were obtained from SQUID measurements. The initial magnetization was randomized, and the relaxed (final) magnetization configuration at zero field was used to obtain the domain periodicity using Fourier analysis. The average periodicity of all 20 magnetic layers, used for comparison with MFM data, was consistent with that of the top layer. Finally, the periodicity trends with

varying A and D were found to be smooth and monotonic, allowing for regression analysis to accurately estimate the DMI magnitude (D_{est}) for each stack composition.

Determining Magnetic Parameters. The saturation magnetisation (M_S) and effective anisotropy, K_{eff}, were determined using SQUID magnetometry measurements in out-of-plane (OP) and in-plane (IP) configurations. The exchange (A_{est}) and DMI (D_{est}) were estimated by χ^2 fit comparisons of the domain periodicity in MFM experiments with micromagnetic simulations. Using the above results, the thermodynamic stability parameter, κ_{est}, was estimated as

$$\kappa_{\text{est}} = (4/\pi) \cdot D_{\text{est}} / \sqrt{A_{\text{est}} \cdot K_{\text{eff}}} \equiv D_{\text{est}} / D_{\text{c}} \, .$$

The evolution of skyrmion configuration with κ_{est} was analysed using Delaunay triangulation techniques (details in §S4).

Magnetic Microscopy and Skyrmion Properties. To determine the domain periodicity, the MTXM and MFM images were analysed in Fourier space. The position and width of the FT peak were used to quantify the domain periodicity and the error bar respectively (Fig. 2k). Meanwhile, the skyrmion sizes ($d_{\text{Sk}}^{\text{MTXM}}$ and $d_{\text{Sk}}^{\text{MFM}}$) were determined by performing 2D isotropic Gaussian fits to skyrmions identified within a $\sim 6 \times 6$ μm^2 field-of-view, with the error bars representative of a true variation in the skyrmion size. The numbers for $d_{\text{Sk}}^{\text{meas}}$ reported here are raw estimates of skyrmion width – no deconvolution has been performed to account for the X-ray point spread function or beam profile, or the MFM tip size. While the $d_{\text{Sk}}^{\text{meas}}$ values reported would systematically overestimate the true skyrmion size, the trends reported as a function of magnetic field (Fig. 2k, Fig. 5c) and sample composition (Fig. 5c-d) are fully conclusive.

* anjans@ntu.edu.sg
† christos@ntu.edu.sg

[1] Dzyaloshinsky, I. A thermodynamic theory of weak ferromagnetism of antiferromagnetics. *Journal of Physics and Chemistry of Solids* **4**, 241–255 (1958).
[2] Moriya, T. Anisotropic Superexchange Interaction and Weak Ferromagnetism. *Physical Review* **120**, 91–98 (1960).
[3] Bogdanov, A. & Hubert, A. Thermodynamically stable magnetic vortex states in magnetic crystals. *Journal of Magnetism and Magnetic Materials* **138**, 255–269 (1994).
[4] Rößler, U. K., Bogdanov, A. N. & Pfleiderer, C. Spontaneous skyrmion ground states in magnetic metals. *Nature* **442**, 797–801 (2006).
[5] Mühlbauer, S. *et al.* Skyrmion lattice in a chiral magnet. *Science* **323**, 915–919 (2009).
[6] Yu, X.-Z. *et al.* Real-space observation of a two-dimensional skyrmion crystal. *Nature* **465**, 901–904 (2010).
[7] Nagaosa, N. & Tokura, Y. Topological properties and dynamics of magnetic skyrmions. *Nature Nanotechnology* **8**, 899–911 (2013).
[8] Fert, A., Cros, V. & Sampaio, J. Skyrmions on the track. *Nature Nanotechnology* **8**, 152–156 (2013).
[9] Sampaio, J., Cros, V., Rohart, S., Thiaville, A. & Fert, A. Nucleation, stability and current-induced motion of isolated magnetic skyrmions in nanostructures. *Nature Nanotechnology* **8**, 839–844 (2013).
[10] Hagemeister, J., Romming, N., von Bergmann, K., Vedmedenko, E. Y. & Wiesendanger, R. Stability of single skyrmionic bits. *Nature Communications* **6**, 8455 (2015).
[11] Heinze, S. *et al.* Spontaneous atomic-scale magnetic skyrmion lattice in two dimensions. *Nature Physics* **7**, 713–718 (2011).
[12] Romming, N. *et al.* Writing and Deleting Single Magnetic Skyrmions. *Science* **341**, 636–639 (2013).
[13] Schulz, T. *et al.* Emergent electrodynamics of skyrmions in a chiral magnet. *Nature Physics* **8**, 301–304 (2012).
[14] Fert, A. Magnetic and Transport Properties of Metallic Multilayers. *Materials Science Forum* **59-60**, 439–480 (1990).
[15] Bode, M. *et al.* Chiral magnetic order at surfaces driven by inversion asymmetry. *Nature* **447**, 190–193 (2007).
[16] Heide, M., Bihlmayer, G. & Blügel, S. Dzyaloshinskii-Moriya interaction accounting for the orientation of magnetic domains in ultrathin films: Fe/W(110). *Physical Review B* **78**, 140403 (2008).
[17] Cho, J. *et al.* Thickness dependence of the interfacial Dzyaloshinskii-Moriya interaction in inversion symmetry broken systems. *Nature Communications* **6**, 7635 (2015).
[18] Dupé, B., Hoffmann, M., Paillard, C. & Heinze, S. Tailoring magnetic skyrmions in ultra-thin transition metal films. *Nature Communications* **5**, 4030 (2014).
[19] Yang, H., Thiaville, A., Rohart, S., Fert, A. & Chshiev, M. Anatomy of Dzyaloshinskii-Moriya Interaction at Co/Pt Interfaces. *Physical Review Letters* **115**, 267210 (2015).
[20] Moreau-Luchaire, C. *et al.* Additive interfacial chiral interaction in multilayers for stabilization of small individual skyrmions at room temperature. *Nature Nanotechnology* **11**, 444–448 (2016).
[21] Woo, S. *et al.* Observation of room-temperature magnetic skyrmions and their current-driven dynamics in ultrathin metallic ferromagnets. *Nature Materials* **15**, 501–506 (2016).
[22] Boulle, O. *et al.* Room-temperature chiral magnetic skyrmions in ultrathin magnetic nanostructures. *Nature Nanotechnology* **11**, 449–454 (2016).
[23] Chen, G., Mascaraque, A., N'Diaye, A. T. & Schmid, A. K. Room temperature skyrmion ground state stabilized through interlayer exchange coupling. *Applied Physics Letters* **106**, 242404 (2015).
[24] Nandy, A. K., Kiselev, N. S. & Blügel, S. Interlayer Exchange Coupling: A General Scheme Turning Chiral Magnets into Magnetic Multilayers Carrying Atomic-Scale Skyrmions. *Physical Review Letters* **116**, 177202 (2016).
[25] Jiang, W. *et al.* Blowing magnetic skyrmion bubbles. *Science* **349**, 283–286 (2015).
[26] Büttner, F. *et al.* Dynamics and inertia of skyrmionic spin structures. *Nature Physics* **11**, 225–228 (2015).
[27] Kiselev, N. S., Bogdanov, A. N., Schäfer, R. & Rößler, U. K. Chiral skyrmions in thin magnetic films: new objects for magnetic storage technologies? *Journal of Physics D: Applied Physics* **44**, 392001 (2011).
[28] Rohart, S. & Thiaville, A. Skyrmion confinement in ultrathin film nanostructures in the presence of Dzyaloshinskii-Moriya interaction. *Physical Review B* **88**, 184422 (2013).

[29] Leonov, A. O. *et al.* The properties of isolated chiral skyrmions in thin magnetic films. *New Journal of Physics* **18**, 065003 (2016).
[30] Tomasello, R. *et al.* A strategy for the design of skyrmion racetrack memories. *Scientific Reports* **4**, 6784 (2014).
[31] Zhang, X., Zhou, Y., Ezawa, M., Zhao, G. P. & Zhao, W. Magnetic skyrmion transistor: skyrmion motion in a voltage-gated nanotrack. *Scientific Reports* **5**, 11369 (2015).
[32] Neubauer, A. *et al.* Topological Hall Effect in the *A* Phase of MnSi. *Physical Review Letters* **102**, 186602 (2009).
[33] Raičević, I. *et al.* Skyrmions in a Doped Antiferromagnet. *Physical Review Letters* **106**, 227206 (2011).
[34] Porter, N. A., Gartside, J. C. & Marrows, C. H. Scattering mechanisms in textured FeGe thin films: Magnetoresistance and the anomalous Hall effect. *Physical Review B* **90**, 024403 (2014).
[35] Milde, P. *et al.* Unwinding of a Skyrmion Lattice by Magnetic Monopoles. *Science* **340**, 1076–1080 (2013).
[36] Dupé, B., Bihlmayer, G., Böttcher, M., Blügel, S. & Heinze, S. Engineering skyrmions in transition-metal multilayers for spintronics. *Nature Communications* **7**, 11779 (2016).
[37] Yang, H., Boulle, O., Cros, V., Fert, A. & Chshiev, M. Controlling Dzyaloshinskii-Moriya Interaction via Chirality Dependent Layer Stacking, Insulator Capping and Electric Field (2016). 1603.01847.
[38] Nagaosa, N., Onoda, S., MacDonald, A. H. & Ong, N. P. Anomalous Hall effect. *Reviews of Modern Physics* **82**, 1539–1592 (2010).
[39] Huang, S. X. & Chien, C. L. Extended Skyrmion Phase in Epitaxial FeGe(111) Thin Films. *Physical Review Letters* **108**, 267201 (2012).
[40] Matsuno, J. *et al.* Interface-driven topological Hall effect in $SrRuO_3$-$SrIrO_3$ bilayer. *Science Advances* **2**, e1600304 (2016).
[41] Song, C.-L. *et al.* Dopant clustering, electronic inhomogeneity, and vortex pinning in iron-based superconductors. *Physical Review B* **87**, 214519 (2013).
[42] Parkin, S. S. P., Hayashi, M. & Thomas, L. Magnetic domain-wall racetrack memory. *Science* **320**, 190–194 (2008).
[43] Kang, W. *et al.* Voltage Controlled Magnetic Skyrmion Motion for Racetrack Memory. *Scientific Reports* **6**, 23164 (2016).
[44] Vansteenkiste, A. *et al.* The design and verification of MuMax3. *AIP Advances* **4**, 107133 (2014).

Acknowledgments. We acknowledge Kevin Masgrau, Shikun He, Bhartendu Satywali, Peter Fischer, and Ophir Auslaender for experimental inputs, and Wen Siang Lew for allowing us to access his instruments. This work was supported by the Singapore Ministry of Education (MoE), Academic Research Fund Tier 2 (Ref. No. MOE2014-T2-1-050), the National Research Foundation (NRF) of Singapore, NRF - Investigatorship (Ref. No.: NRF-NRFI2015-04), and the A*STAR Pharos Fund (Ref. No. 1527400026) of Singapore. The X-ray microscopy work at ALS was supported by Leading Foreign Research Institute Recruitment Program through the National Research Foundation of Korea, funded by the Ministry of Education, Science and Technology (MEST) (Ref. No. 2012K1A4A3053565 and 2014R1A2A2A01003709).

Author Contributions. A.S., M.T., F.E., and C.P. designed and initiated the research. M.R. deposited the films, and characterised them with A.S. M.Y.I. conducted the MTXM experiments. A.K.C.T. performed the MFM experiments and analysed the imaging data with A.S., and P.H. validated the MFM results. M.R. and A.P.P. performed transport experiments and analysed the data. A.L.G.O. performed micromagnetics simulations. K.H.K. and C.K.G. carried out the DFT calculations. A.S. and C.P. coordinated the project and wrote the manuscript. All authors discussed the results and provided inputs to the manuscript.